LETTER

https://doi.org/10.1038/s41586-019-0975-z

Evidence for moiré excitons in van der Waals heterostructures

Kha Tran[1,11], Galan Moody[2,11], Fengcheng Wu[3]*, Xiaobo Lu[4], Junho Choi[1], Kyounghwan Kim[5], Amritesh Rai[5], Daniel A. Sanchez[6], Jiamin Quan[1], Akshay Singh[1,10], Jacob Embley[1], André Zepeda[1], Marshall Campbell[1], Travis Autry[2], Takashi Taniguchi[7], Kenji Watanabe[7], Nanshu Lu[6,8], Sanjay K. Banerjee[5], Kevin L. Silverman[2], Suenne Kim[9], Emanuel Tutuc[5], Li Yang[4], Allan H. MacDonald[1] & Xiaoqin Li[1,6]*

Recent advances in the isolation and stacking of monolayers of van der Waals materials have provided approaches for the preparation of quantum materials in the ultimate two-dimensional limit[1,2]. In van der Waals heterostructures formed by stacking two monolayer semiconductors, lattice mismatch or rotational misalignment introduces an in-plane moiré superlattice[3]. It is widely recognized that the moiré superlattice can modulate the electronic band structure of the material and lead to transport properties such as unconventional superconductivity[4] and insulating behaviour driven by correlations[5–7]; however, the influence of the moiré superlattice on optical properties has not been investigated experimentally. Here we report the observation of multiple interlayer exciton resonances with either positive or negative circularly polarized emission in a molybdenum diselenide/tungsten diselenide ($MoSe_2/WSe_2$) heterobilayer with a small twist angle. We attribute these resonances to excitonic ground and excited states confined within the moiré potential. This interpretation is supported by recombination dynamics and by the dependence of these interlayer exciton resonances on twist angle and temperature. These results suggest the feasibility of engineering artificial excitonic crystals using van der Waals heterostructures for nanophotonics and quantum information applications.

In van der Waals materials the usual constraint of lattice matching between adjacent layers is lifted, enabling different types of materials to be stacked to form atomically thin heterostructures. The twist angle between two layers can be adjusted arbitrarily, in contrast to conventional epitaxially grown heterostructures in which the orientation of adjacent layers is fixed by the crystal axes. These unique properties of van der Waals heterostructures present new possibilities to engineer the electronic band structure and optical properties via the formation of an in-plane moiré superlattice. The vertical stacking of two monolayers of semiconducting transition-metal dichalcogenides (TMDs) does not necessarily give rise to a moiré superlattice. The lattice constants of TMDs that share common chalcogen atoms (for example MoX_2 and WX_2) differ only by about 0.1%. In rotationally aligned $MoSe_2/WSe_2$ heterobilayers grown by chemical vapour deposition methods, the minor lattice distortion in each layer leads to a commensurate atomic alignment without a moiré pattern[8]. In mechanically stacked heterobilayers, however, there is usually a twist angle between the two layers. Thus a moiré pattern is expected, and indeed has been directly imaged with high-resolution transmission electron microscopy[9].

In TMD heterobilayers with a typical type-II band alignment[10–12], the rapid charge transfer[13] of electrons and holes to different layers after optical excitation leads to emission from the lower-energy interlayer exciton transitions[14,15]. Theoretically, multiple interlayer exciton resonances are expected to form owing to the lateral confinement from the moiré potential[16–18] (Fig. 1). The interlayer coupling determines the depth of the moiré potential that, in TMD heterobilayers, is predicted to be approximately 100–200 meV from first-principles calculations (see Methods and Extended Data Fig. 1); this has been confirmed by scanning tunnelling spectroscopy experiments on a rotationally aligned MoS_2/WSe_2 bilayer grown by chemical vapour deposition[3]. Such a deep potential is expected to localize interlayer excitons provided that the moiré supercell has a period of the order of 10 nm or larger[16,18]. Whether and how the moiré potential manifests in far-field diffraction-limited optical measurements remains an unanswered question.

Here we report the observation of multiple interlayer exciton resonances in a high-quality hexagonal boron nitride (hBN)-encapsulated $MoSe_2/WSe_2$ heterobilayer. The layers are aligned with a small twist angle and the inhomogeneous spectral linewidths are reduced in the presence of the hBN capping layers, resulting in several nearly equally spaced interlayer exciton resonances being spectrally resolved at low temperature. Upon excitation with σ^+ circularly polarized light, the interlayer exciton resonances exhibit alternating co- and cross-circularly polarized photoluminescence. We suggest that the alternating polarized emission originates from the atomic-scale spatial variations of the optical selection rules within a moiré supercell. The energy spacing, the twist-angle dependence of the resonances and the helicity of the emitted light are consistent with calculations of multiple interlayer exciton states that are laterally confined within a moiré potential of approximately 150 meV, in agreement with first-principles calculations. Time-resolved and temperature-dependent photoluminescence measurements support this assignment of the ground- and excited-state interlayer excitons.

We first describe conceptually how the moiré potential may give rise to multiple exciton resonances with different optical selection rules (Fig. 1). In $MoSe_2/WSe_2$ heterobilayers with a small twist angle (approximately 1°), the exciton Bohr radius is large compared to the monolayer lattice constant but small relative to the moiré period (about 20 nm). Thus, the interlayer exciton can be described as a particle moving in a slowly varying moiré potential[18,19]. Within a moiré supercell, there are three points at which the local atomic registration preserves the three-fold rotational symmetry $\hat{C}_3$, as shown in Fig. 1a, b. These three sites are denoted by R_h^h, R_h^X and R_h^M, where R_h^μ refers to R-type stacking in which the μ site of the $MoSe_2$ layer aligns with the hexagon centre (h) of the WSe_2 layer. These high-symmetry points are local energy extrema within the moiré supercell in which excitons can be localized. In the case of sufficiently deep energy modulation, the moiré pattern can provide an array of identical quantum-dot potentials (Fig. 1c).

[1]Department of Physics and Center for Complex Quantum Systems, The University of Texas at Austin, Austin, TX, USA. [2]National Institute of Standards & Technology, Boulder, CO, USA. [3]Materials Science Division, Argonne National Laboratory, Argonne, IL, USA. [4]Department of Physics, Washington University in St Louis, St Louis, MO, USA. [5]Microelectronics Research Center, Department of Electrical and Computer Engineering, The University of Texas at Austin, Austin, TX, USA. [6]Texas Materials Institute, The University of Texas at Austin, Austin, TX, USA. [7]National Institute of Material Science, Tsukuba, Japan. [8]Department of Aerospace Engineering and Engineering Mechanics, The University of Texas at Austin, Austin, TX, USA. [9]Department of Photonics and Nanoelectronics and Department of Applied Physics, Hanyang University, Ansan, South Korea. [10]Present address: Department of Material Science and Engineering, Massachusetts Institute of Technology, Cambridge, MA, USA. [11]These authors contributed equally: Kha Tran, Galan Moody. *e-mail: wufcheng@gmail.com; elaineli@physics.utexas.edu

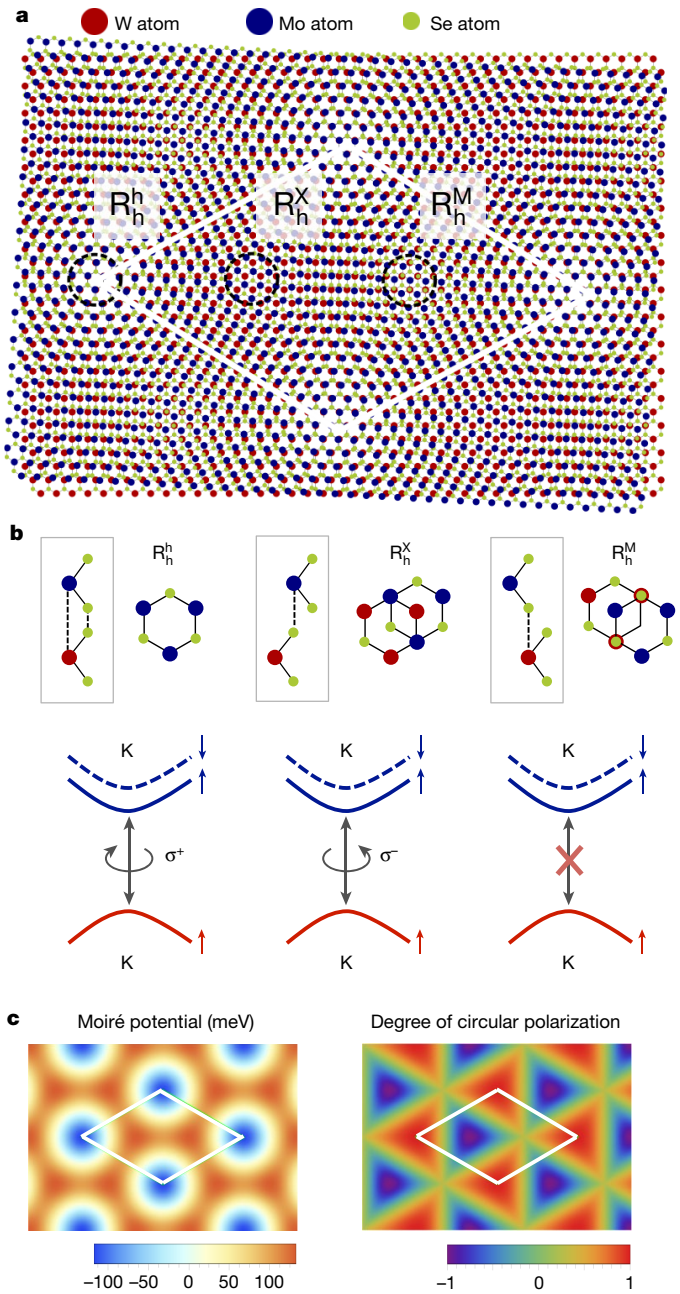

Fig. 1 | Moiré superlattice modulates the electronic and optical properties. a, Different local atomic alignments occur in a $MoSe_2/WSe_2$ vertical heterostructure with a small twist angle. The three highlighted regions correspond to local atomic configurations with three-fold rotational symmetry. **b**, In the K valley, $S_z = 0$ interlayer exciton transitions occur between spin-up conduction-band electrons in the $MoSe_2$ layer and spin-up valence-band electrons in the WSe_2 layer. K-valley excitons obey different optical selection rules depending on the atomic configuration R_h^μ within the moiré pattern. R_h^μ refers to R-type stacking with the μ site of the $MoSe_2$ layer aligning with the hexagon centre (h) of the WSe_2 layer. Exciton emission at R_h^h (R_h^X) is left-circularly (right-circularly) polarized. Emission from the R_h^M site is dipole-forbidden for normal incidence. **c**, Left, the moiré potential of the interlayer exciton transition, showing a local minimum at the R_h^h site. Right, spatial map of the optical selection rules for K-valley excitons. The high-symmetry points are circularly polarized and the regions in between are elliptically polarized.

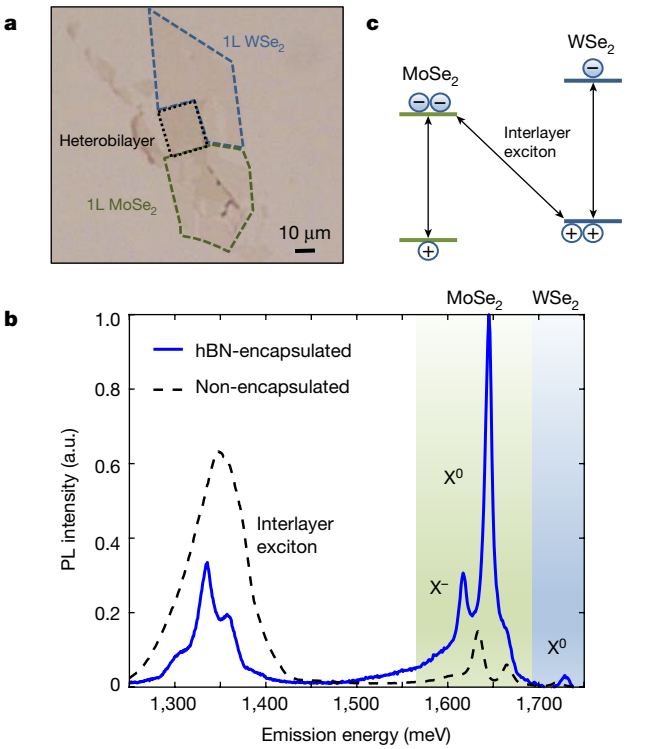

Fig. 2 | Photoluminescence from $MoSe_2/WSe_2$ heterobilayer with 1° twist angle. a, Optical image of a hBN-encapsulated $MoSe_2/WSe_2$ stacked heterostructure. The heterobilayer region is indicated inside the black dotted line. **b**, Comparison of the photoluminescence spectrum from an uncapped heterostructure (dashed black curve) and a hBN-encapsulated heterostructure (solid blue curve). Neutral (X^0) and charged (X^-) exciton emission is observed from the $MoSe_2$ and WSe_2 monolayers. The interlayer exciton emission is observed approximately 300 meV below the intralayer resonances. **c**, Illustrative band diagram showing the type-II alignment and the interlayer exciton transition. a.u., arbitrary units.

Another important effect of the moiré pattern is to impose spatially varying optical selection rules[18,20]. Although the valley degree of freedom is still a good quantum number for interlayer excitons, the optical selection rules of exciton resonances are no longer locked to the valley index, as is the case in monolayers. As shown in Fig. 1b, an exciton residing directly at site R_h^h (R_h^X) couples only to σ^+ (σ^-) polarized light. The dipole of site R_h^M is oriented perpendicular to the plane and does not couple efficiently to normal incident light (see Methods). The optical selection rules are determined not only by atomic quantum numbers, but also by the relative position between tungsten and molybdenum atoms in real space. It is the latter dependence that is responsible for distinct selection rules at different positions within the moiré supercell. The optical selection rules change continuously in the moiré pattern and are generally elliptically polarized (Fig. 1c).

To examine the influence of the moiré potential on interlayer excitons, we performed micro-photoluminescence measurements on multiple $MoSe_2/WSe_2$ heterobilayers. The samples were prepared following a mechanical exfoliation and transfer process[21]. We focus on one hBN-encapsulated heterobilayer with a twist angle of 1° unless otherwise stated (see Methods and Extended Data Fig. 2). Figure 2a shows an optical microscopy image of this heterobilayer. The sample was held at 15 K and excited with a continuous-wave 660-nm laser with a full-width at half-maximum spot size of 1.5 μm. The photoluminescence spectrum of a non-encapsulated sample (dashed curve in Fig. 2b) features intralayer neutral and charged excitons and a broad interlayer exciton resonance, consistent with earlier reports[14,22,23]. When the heterobilayer is encapsulated between hBN layers, four spectrally resolved interlayer exciton resonances emerge (solid curve in Fig. 2b) owing to reduced inhomogeneous broadening. The spectral region of the interlayer exciton is replotted in the lower panel of Fig. 3a and fitted with four Gaussian functions. The central emission energies extracted from the fits are 1,311 meV, 1,335 meV, 1,355 meV and 1,377 meV. The resonance energies are repeatable across different locations on the heterobilayer with an almost constant peak spacing of 22 ± 2 meV

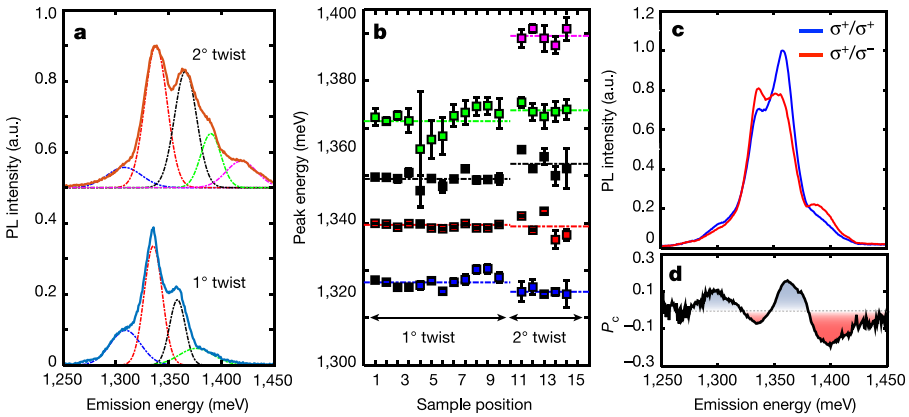

Fig. 3 | Twist-angle dependence and circularly polarized emission. **a**, Representative photoluminescence spectra shown for heterobilayers with twist angles of 1° (bottom) and 2° (top). Each spectrum is fitted with four (1°) or five (2°) Gaussian functions. **b**, The centre energy of each peak obtained from the fits at different spatial positions across each sample. The average peak spacing increases from 22 ± 2 meV to 27 ± 3 meV as the twist angle increases from 1° to 2°. **c**, Circularly polarized photoluminescence spectrum for σ^+ excitation of the 1° sample. **d**, The degree of circular polarization plotted against the emission wavelength obtained from the spectra in **c**.

(Fig. 3b). Some moderate inhomogeneous broadening remains, possibly due to multiple moiré domains or small variations in strain and layer spacing within the excitation spot, which covers around 1,000 moiré supercells.

Multiple interlayer exciton peaks may be indicative of quantized energy levels arising from the lateral confinement imposed by the moiré potential, as predicted in the calculations below. The fact that the resonances span an energy range of about 70 meV suggests that the moiré potential depth is of the order of 100 meV—sufficient to justify the picture of an array of quantum-dot potentials. Polarization-resolved photoluminescence experiments provide additional compelling evidence in support of this interpretation. By using σ^+ polarized excitation, we collected co- (σ^+ detection) and cross- (σ^- detection) circularly polarized photoluminescence spectra, which are shown in Fig. 3c. We define the circular polarization of emission as $P_c = \frac{I_{co} - I_{cross}}{I_{co} + I_{cross}}$, where I is the measured photoluminescence intensity. The plot of P_c as a function of energy is shown in Fig. 3d. The values of P_c for the interlayer exciton resonances vary between 0.2 and −0.2. A negative P_c indicates that the photoluminescence signal with cross-circular polarization is stronger than that from the co-circular polarization. We propose that the alternating co- and cross-circular emission arises from the unique spatial variation of the optical selection rules predicted on the basis of rotational symmetry considerations[18].

To relate the observed photoluminescence signal to the optical selection rules, we first assume that the above-gap, σ^+-polarized light optically creates spin-polarized intralayer excitons in the $MoSe_2$ and WSe_2 monolayers primarily in the K valley. This spin-valley locking in TMD monolayers has been established by previous studies[24–26]. Second, we assume that the charge-transfer process that leads to the formation of interlayer excitons conserves the valley and spin indices, an assumption that is supported by data from polarization-resolved pump–probe spectroscopy in a previous study[27]. It then follows that an interlayer exciton state generated in the K valley after σ^+ optical excitation emits σ^+ (σ^-) polarized light if it is localized near the R_h^h (R_h^X) high-symmetry point within the moiré potential landscape (Fig. 1b, c). The calculations below show that, for a deep moiré potential that confines excitons at the R_h^h site, the wavefunctions associated with the quantized exciton states can acquire additional angular momentum and sample the potential landscape in a way that leads to multiple resonances with alternating σ^+ and σ^- light emission—a characteristic consistent with our experimental observations. Because the valley-relaxation and charge-transfer dynamics can be very complex, the above assumptions do not strictly hold, leading to reduced P_c below unity. Because observing the alternating circular selection rules of interlayer exciton resonances requires that the valley polarization time is longer than or comparable to interlayer exciton recombination lifetimes[25], valley-conserving photoluminescence can only be observed in bilayers with the smallest (1°) twist angle, which exhibit relatively short interlayer exciton recombination lifetimes (around 1 ns).

Theoretically, multiple quantized resonances originating from the ground- and excited-state interlayer excitons can exhibit alternating selection rules owing to the moiré superlattice. The Bohr radius of an interlayer exciton (around 1 nm) is substantially smaller than the moiré period, enabling the interlayer exciton to be treated as a composite quasiparticle with a wavepacket moving in the potential. Its centre-of-mass motion is described by

$$H = \hbar\Omega_0 + \frac{\hbar^2 \boldsymbol{k}^2}{2M} + \Delta(\boldsymbol{r}) \quad (1)$$

where $\hbar\Omega_0$ is an energy constant, $\hbar^2\boldsymbol{k}^2/(2M)$ is the centre-of-mass kinetic energy, $\Delta(\boldsymbol{r})$ is the exciton moiré potential energy and M is the exciton mass. Because $\Delta(\boldsymbol{r})$ varies smoothly, it can be approximated by the lowest-order harmonic expansion and is then specified completely by one strength and one shape parameter. On the basis of the experiments, we adjust the shape parameter to place the minima of $\Delta(\boldsymbol{r})$ at these sites. Near R_h^h sites, $\Delta(\boldsymbol{r})$ has the form of a harmonic oscillator with quantized energy levels controlled by the moiré period a_M. We take the twist angle to be 1°, resulting in a value of a_M of around 19 nm.

Both +K and −K valley excitons are governed by the Hamiltonian in equation (1), but they have different optical responses due to valley-dependent optical selection rules. Below we focus on +K valley excitons; properties of −K valley excitons can be inferred by using time-reversal symmetry. At each spatial position, the interlayer optical matrix element $\boldsymbol{J}(\boldsymbol{r})$ can be written as $J^+(\boldsymbol{r})\hat{\boldsymbol{e}}^+ + J^-(\boldsymbol{r})\hat{\boldsymbol{e}}^-$, where $J^+(\boldsymbol{r})$ ($J^-(\boldsymbol{r})$) corresponds to σ^+ (σ^-) components. There are three notable positions with high symmetry: $\boldsymbol{J}(\boldsymbol{r})$ has a pure σ^+ component at R_h^h sites, a pure σ^- component at R_h^X sites, and vanishes at R_h^M sites. Around the R_h^h site ($\boldsymbol{r} = 0$), $J^+(\boldsymbol{r})$ is almost constant whereas $J^-(\boldsymbol{r})$ has a vortex structure: $J^-(\boldsymbol{r}) \propto r_x - ir_y$. A description of the spatial variation of $J^+(\boldsymbol{r})$ and $J^-(\boldsymbol{r})$ is provided in Methods and shown in Extended Data Fig. 3.

More than one interlayer exciton resonance can be accommodated in a deep moiré potential, as illustrated in Fig. 4a. On the basis of equation (1), we calculate the theoretical optical conductivity of +K valley interlayer excitons, as shown in Fig. 4b. Four resonances with alternating optical selection rules appear within the energy range of the potential. The corresponding exciton centre-of-mass wavefunction can be understood as Bloch wave states composed of Wannier functions confined to the potential minimum position (R_h^h sites). In Fig. 4c–e, we illustrate the centre-of-mass wavefunctions of the first three resonances. Resonance 1 has s-wave symmetry centred at the R_h^h site, and its optical

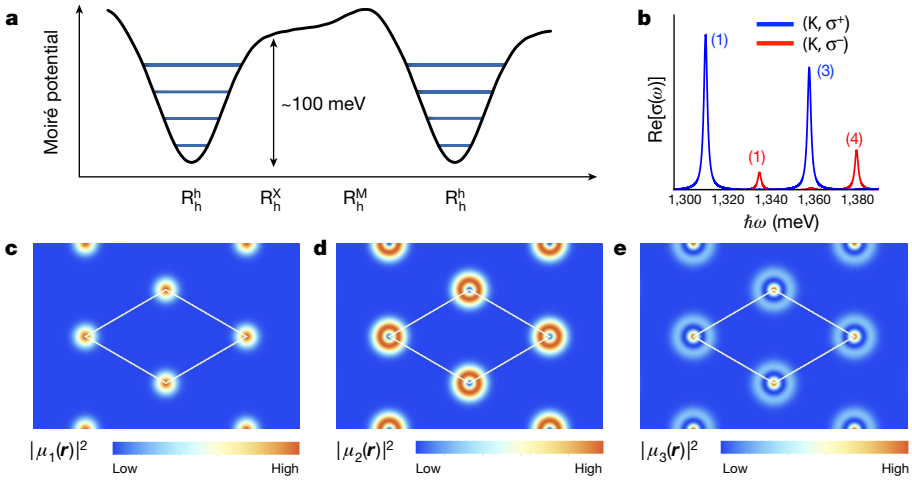

Fig. 4 | Calculated multiple interlayer exciton resonances confined in a moiré supercell. a, Illustration of the spatial variation of the moiré potential and the confined multiple interlayer exciton resonances. **b**, Optical conductivity of interlayer excitons in the K valley in response to σ^+ (blue line) and σ^- (red line) polarized light. **c**–**e**, Real-space map of the centre-of-mass wavefunctions for peaks 1, 2 and 3, respectively.

matrix element has only σ^+ components. The wavefunction of resonance 2 is also centred at the R^h_h site, but it has a chiral p-waveform with an additional angular momentum. Owing to this difference between the wavefunctions of resonances 1 and 2, their optical selection rules have opposite helicity. The behaviour of resonances 3 and 4—which have d- and f-waveforms, respectively—can be understood in a similar way. As expected, our model calculation cannot reproduce all of the features observed experimentally, such as the linewidths and relative intensity between the interlayer exciton resonances. For example, the photoluminescence intensity of the excited states is higher than that of the ground state, a feature that may originate from disorder and has been previously observed in an ensemble of self-assembled quantum dots[28]. The assignment of the observed interlayer exciton peaks as ground and excited states localized near the moiré potential minimum is consistent with the measured thermal behaviour and recombination dynamics (Methods, Extended Data Fig. 4).

A natural choice for the control of moiré excitons would be to tune the moiré period through the twist angle. Indeed, in another heterobilayer with a small twist angle of approximately 2°, we observed multiple interlayer exciton resonances spaced by 27 ± 3 meV; as expected, this is larger than the spacing for the 1° sample (Fig. 3, Extended Data Fig. 5). Although systematic studies of the twist-angle dependence of interlayer excitons in TMD heterobilayers have been performed for large steps (around 5°)[29,30], the broad inhomogeneous linewidth has precluded observation of the effect of the moiré potential. An applied electric field or magnetic field may also enable tuning of the properties of interlayer excitons. Previous experiments have reported that interlayer excitons exhibit a Stark shift as a function of an applied electric field[31] or a Zeeman splitting as function of an applied magnetic field[23,31]. Other recent experiments have also reported multiple interlayer exciton resonances. However, these experiments were performed on samples either with different stacking conditions[31,32] (see Methods and Extended Data Fig. 6) or with considerably broader interlayer exciton inhomogeneous linewidths that mask any effects of the moiré potential[29,30]. We also discuss the possible contribution from $S_z = 1$ transitions (Methods), which are optically dark in monolayers but become bright in heterobilayers.

In summary, we observed multiple interlayer exciton resonances in a hBN-encapsulated $MoSe_2/WSe_2$ heterobilayer. We explain the key spectroscopic features observed in our experiments—four interlayer exciton resonances with alternating circularly polarized photoluminescence, systematic changes in the lifetime with energy, and temperature dependence—by assuming the presence of a moiré superlattice, the existence of which is expected in a stacked heterobilayer. In multiple samples with slightly different twist angles, we observed systematic changes in the energy spacing and lifetime of the interlayer excitons, which is consistent with the effect of the moiré potential. Multiple interlayer exciton resonances originating from phonon replicas[33], momentum-space indirect transitions[32], or $S_z = 1$states are possible in TMD bilayers; however, we consider them less likely explanations in the samples investigated here. Experiments capable of resolving individual interlayer excitons confined within a supercell, using either near-field optical probe or combined scanning tunnelling spectroscopy and optical spectroscopy studies, will be valuable to further establish the influence of the moiré potential.

Online content

Any methods, additional references, Nature Research reporting summaries, source data, statements of data availability and associated accession codes are available at https://doi.org/10.1038/s41586-019-0975-z.

Received: 30 April 2018; Accepted: 20 December 2018;
Published online: 25 February 2019

1. Li, M.-Y., Chen, C.-H., Shi, Y. & Li, L.-J. Heterostructures based on two-dimensional layered materials and their potential applications. *Mater. Today* **19**, 322–335 (2016).
2. Liu, Y. et al. Van der Waals heterostructures and devices. *Nat. Rev. Mater.* **1**, 16042 (2016).
3. Zhang, C. et al. Interlayer couplings, Moiré patterns, and 2D electronic superlattices in MoS_2/WSe_2 hetero-bilayers. *Sci. Adv.* **3**, e1601459 (2017).
4. Cao, Y. et al. Unconventional superconductivity in magic-angle graphene superlattices. *Nature* **556**, 43–50 (2018).
5. Hunt, B. et al. Massive Dirac fermions and Hofstadter butterfly in a van der Waals heterostructure. *Science* **340**, 1427–1430 (2013).
6. Dean, C. R. et al. Hofstadter's butterfly and the fractal quantum Hall effect in moiré superlattices. *Nature* **497**, 598–602 (2013).
7. Kim, K. et al. Tunable moiré bands and strong correlations in small-twist-angle bilayer graphene. *Proc. Natl Acad. Sci. USA* **114**, 3364–3369 (2017).
8. Hsu, W.-T. et al. Negative circular polarization emissions from $WSe_2/MoSe_2$ commensurate heterobilayers. *Nat. Commun.* **9**, 1356 (2018).
9. van der Zande, A. M. et al. Tailoring the electronic structure in bilayer molybdenum disulfide via interlayer twist. *Nano Lett.* **14**, 3869–3875 (2014).
10. Kang, J., Tongay, S., Zhou, J., Li, J. & Wu, J. Band offsets and heterostructures of two-dimensional semiconductors. *Appl. Phys. Lett.* **102**, 012111 (2013).
11. Kośmider, K. & Fernández-Rossier, J. Electronic properties of the MoS_2-WS_2 heterojunction. *Phys. Rev. B* **87**, 075451 (2013).
12. Chiu, M.-H. et al. Determination of band alignment in the single-layer MoS_2/WSe_2 heterojunction. *Nat. Commun.* **6**, 7666 (2015).
13. Hong, X. et al. Ultrafast charge transfer in atomically thin MoS_2/WS_2 heterostructures. *Nat. Nanotechnol.* **9**, 682–686 (2014).
14. Rivera, P. et al. Observation of long-lived interlayer excitons in monolayer $MoSe_2$–WSe_2 heterostructures. *Nat. Commun.* **6**, 6242 (2015).
15. Gong, Y. et al. Vertical and in-plane heterostructures from WS_2/MoS_2 monolayers. *Nat. Mater.* **13**, 1135–1142 (2014).
16. Wu, F., Lovorn, T. & MacDonald, A. H. Theory of optical absorption by interlayer excitons in transition metal dichalcogenide heterobilayers. *Phys. Rev. B* **97**, 035306 (2018).
17. Wu, F., Lovorn, T. & MacDonald, A. H. Topological exciton bands in moiré heterojunctions. *Phys. Rev. Lett.* **118**, 147401 (2017).

18. Yu, H., Liu, G.-B., Tang, J., Xu, X. & Yao, W. Moiré excitons: From programmable quantum emitter arrays to spin-orbit-coupled artificial lattices. *Sci. Adv.* **3**, e1701696 (2017).
19. Gillen, R. & Maultzsch, J. Interlayer excitons in $MoSe_2$/WSe_2 heterostructures from first principles. *Phys. Rev. B* **97**, 165306 (2018).
20. Yu, H., Wang, Y., Tong, Q., Xu, X. & Yao, W. Anomalous light cones and valley optical selection rules of interlayer excitons in twisted heterobilayers. *Phys. Rev. Lett.* **115**, 187002 (2015).
21. Andres, C.-G. et al. Deterministic transfer of two-dimensional materials by all-dry viscoelastic stamping. *2D Mater.* **1**, 011002 (2014).
22. Philipp, N. et al. Interlayer exciton dynamics in a dichalcogenide monolayer heterostructure. *2D Mater.* **4**, 025112 (2017).
23. Nagler, P. et al. Giant magnetic splitting inducing near-unity valley polarization in van der Waals heterostructures. *Nat. Commun.* **8**, 1551 (2017).
24. Zeng, H., Dai, J., Yao, W., Xiao, D. & Cui, X. Valley polarization in MoS_2 monolayers by optical pumping. *Nat. Nanotechnol.* **7**, 490–493 (2012).
25. Mak, K. F., He, K., Shan, J. & Heinz, T. F. Control of valley polarization in monolayer MoS_2 by optical helicity. *Nat. Nanotechnol.* **7**, 494–498 (2012).
26. Tran, K. et al. Disorder-dependent valley properties in monolayer WSe_2. *Phys. Rev. B* **96**, 041302 (2017).
27. Schaibley, J. R. et al. Directional interlayer spin-valley transfer in two-dimensional heterostructures. *Nat. Commun.* **7**, 13747 (2016).
28. Torchynska, T. V., Dybiec, M. & Ostapenko, S. Ground and excited state energy trend in InAs/InGaAs quantum dots monitored by scanning photoluminescence spectroscopy. *Phys. Rev. B* **72**, 195341 (2005).
29. Kunstmann, J. et al. Momentum-space indirect interlayer excitons in transition-metal dichalcogenide van der Waals heterostructures. *Nat. Phys.* **14**, 801–805 (2018).
30. Nayak, P. K. et al. Probing evolution of twist-angle-dependent interlayer excitons in $MoSe_2$/WSe_2 van der Waals heterostructures. *ACS Nano* **11**, 4041–4050 (2017).
31. Ciarrocchi, A. et al. Polarization switching and electrical control of interlayer excitons in two-dimensional van der Waals heterostructures. *Nat. Photonics* **13**, 131–136 (2018).
32. Hanbicki, A. T. et al. Double indirect interlayer exciton in a $MoSe_2$/WSe_2 van der Waals heterostructure. *ACS Nano* **12**, 4719–4726 (2018).
33. Wang, Z., Chiu, Y.-H., Honz, K., Mak, K. F. & Shan, J. Electrical tuning of interlayer exciton gases in WSe_2 bilayers. *Nano Lett.* **18**, 137–143 (2018).

Acknowledgements The work performed by K.T., J.C., A.H.M. and X. Li was primarily supported by the National Science Foundation (NSF) through the Center for Dynamics and Control of Materials, an NSF MRSEC, under Cooperative Agreement DMR-1720595. X. Li also acknowledges partial support from NSF EFMA-1542747 and the Welch Foundation via grant F-1662. The theoretical work by F.W. was supported by the US Department of Energy, Office of Science, Basic Energy Sciences, Materials Sciences and Engineering Division. J.Q acknowledges support from the China Scholarship Council (grant 201706050068). A.H.M., K.K. and E.T. were supported in part by Army Research Office (ARO) grant W911NF-17-1-0312 (MURI). X. Lu and L.Y. are supported by the Air Force Office of Scientific Research (AFOSR) FA9550-17-1-0304 and NSF DMR-1455346. S.K. was financially supported by National Research Foundation of Korea (NRF) grant funded by the South Korean government (2017R1D1B04036381). K.W. and T.T. acknowledge support from the Elemental Strategy Initiative conducted by the MEXT, Japan and JSPS KAKENHI grant JP15K21722. A.R. and S.K.B. acknowledge support from the NASCENT Engineering Research Centre (ERC) funded by NSF grant EEC-1160494. D.A.S acknowledges support from the NSF Graduate Research Fellowship Program. N.L. acknowledges support from NSF CMMI-1351875. The Texas Nanofabrication Facility, where some of the work was carried out, is a member of the National Nanotechnology Coordinated Infrastructure, which is supported by the NSF (grant ECCS-1542159). This work is an official contribution of NIST, which is not subject to copyright in the United States.

Author contributions K.T. and G.M. performed the steady-state and time-resolved optical measurements. F.W. and X. Lu performed the calculations. K.T., J.C., J.E., A.Z., M.C., T.T. and K.W. prepared the samples. A.S., K.K., A.R., T.A., J.Q. and D.A.S. assisted with the experiments. K.T., G.M., F.W. and X. Li wrote the manuscript. E.T., S.K.B., N.L., K.L.S., S.K., L.Y., A.H.M. and X. Li supervised the project. All authors discussed the results and commented on the manuscript at all stages.

Competing interests The authors declare no competing interests.

Additional information
Extended data is available for this paper at https://doi.org/10.1038/s41586-019-0975-z.
Reprints and permissions information is available at http://www.nature.com/reprints.
Correspondence and requests for materials should be addressed to F.W. or X.L.
Publisher's note: Springer Nature remains neutral with regard to jurisdictional claims in published maps and institutional affiliations.

METHODS

Sample preparation. The $MoSe_2$ and WSe_2 monolayers and hexagonal boron nitride (hBN) capping layers were prepared by mechanical exfoliation onto a polydimethylsiloxane sheet. The heterobilayer was constructed layer by layer using the all-dry viscoelastic stamping method[21]. No chemical was in contact with the layers during transfer. The bottom hBN was first transferred onto a sapphire substrate, followed by the WSe_2 monolayer. The top $MoSe_2$ monolayer was then stacked above the WSe_2 monolayer such that the crystal axes were rotationally aligned with a precision better than 1°. Polarization- and phase-resolved second-harmonic generation measurements were used to determine the crystal axes of the two monolayers[34–36]. Finally, a thin hBN layer (around 15-nm thick) was deposited on top of the heterobilayer. A microscopic picture of one sample is shown in Fig. 2a without the top hBN layer for clarity. The sample was annealed after every step during the transfer process under ultrahigh vacuum (around 10^{-5} mbar) at 200 °C for 8 hours.

Optical spectroscopy. For steady-state photoluminescence measurements, the sample was held at 15 K and excited using a continuous-wave 660-nm laser focused to a spot size of 1.5 μm using a long working distance microscope objective with a numerical aperture of 0.42. The transmitted photoluminescence signal was dispersed through a spectrometer and detected by a charge-coupled device. For time-resolved photoluminescence measurements, a Ti:sapphire-pumped optical parametric oscillator emitting 100-fs, 680-nm pulses at a 76-MHz repetition rate was used as the excitation source. The photoluminescence was spectrally filtered with a 1-nm bandwidth using a monochromator, and detected using a single-photon avalanche detector and time-tagging electronics. The steady-state and time-resolved photoluminescence data were acquired using an average power of 100 μW. No qualitative change in the spectra or dynamics was observed for powers down to 1 μW.

First-principles calculation of the bandgaps of the $MoSe_2/WSe_2$ bilayer heterostructure. We used density functional theory (DFT) with the Perdew–Burke–Ernzerh (PBE) exchange-correlation functional including spin–orbit coupling to calculate the electronic structure of three specific stacking types within the moiré superlattices in a twisted $MoSe_2/WSe_2$ heterobilayer (Extended Data Fig. 1). The interlayer van der Waals interaction is included within the DFT-D2 functional implemented in the Vienna ab initio simulation package (VASP) package[37,38]. The cutoff of plane-wave energy was set to be 500 eV with a $16 \times 16 \times 1$ k-point sampling in the reciprocal space. The atomic structures were calculated with a perpendicular vacuum larger than 18 Å, which is sufficient to avoid artificial interactions between adjacent supercells. Because of the strong spin–orbit splitting at the +K/−K point, the band structures of the three stacking types exhibit a direct bandgap at the +K/−K point, as shown in Extended Data Fig. 1. Therefore, without considering phonons, we expect the lowest-energy interlayer exciton to be a direct exciton. Extended Data Fig. 1 shows the relaxed interlayer distances and bandgap values which are substantially different with different stacking types and are sensitive to the interlayer couplings. Van der Waals interactions are the consequence of dynamical correlation effects which may not be well captured by DFT. To evaluate possible variations, we performed additional calculations using another van der Waals functional, the DFT-D3, in which the interlayer distances and bandgaps are different. Despite different choices of van der Waals functionals, the bandgaps varied more than 100 meV between different stacking types within the moiré superlattice; that is, a deep moiré potential was consistently found in the first-principle calculations. Because electron self-energy corrections and excitonic effects are known to dominate quasiparticle bandgaps and optical spectra of 2D semiconductors, we applied the first-principles GW-Bethe–Salpeter Equation (BSE) to obtain the energy of the lowest exciton (L.Y. and X. Lu, unpublished results). The quasiparticle energies were calculated by the single-shot G_0W_0 approximation using the general plasmon pole model. We used a k-point grid of $24 \times 24 \times 1$ for calculating the electron–hole interaction kernel and a k-point grid of $48 \times 48 \times 1$ for converged excitonic states. These GW-BSE simulations were performed using the BerkeleyGW code with the slab Coulomb truncation included. It was found that the exciton binding energy varies less than 5% within the moiré supercell. Our calculations also confirmed that the moiré potential depth (that is, the quasiparticle gap) in H-stacked samples (~20 meV) was considerably reduced compared to that in R-stacked samples (>100 meV).

Polarization- and phase-resolved second-harmonic-generation measurements. We first determined the monolayer zigzag and armchair direction by measuring the polarization-resolved second-harmonic generation (SHG) following a method described elsewhere[34,35]. We used the output of a Ti:sapphire laser with the centre wavelength at 800 nm (ω) and a pulse duration of around 100 fs. The laser was focused onto the sample using a 10× objective, which generates an SHG signal ($2\omega_{sample}$) at 400 nm. The laser power at the sample was around 5 mW with a spot size of diameter 5 μm. The second harmonic signal (400 nm) then passes through the analyser, which is linearly cross-polarized with respect to the excitation laser (800 nm). As the sample is rotated in a plane normal to the incident laser direction, the polarization resolved SHG signal is six-fold degenerate as shown in Extended Data Fig. 2a. The peaks of the curves correspond to the armchair directions of the monolayer. To distinguish monolayers rotated by 60°, we used phase-resolved SHG as described previously[36,39,40] and shown in Extended Data Fig. 2b. Two interference spectra were plotted on top of each other for comparison. If the spectra are in phase (out of phase) as shown in Extended Data Fig. 2c (Extended Data Fig. 2d), the two stacked monolayers will have a twist angle close to 0° (60°).

Calculations of the moiré potential and interlayer exciton optical response. Here we provide a detailed description of the theory, which has some overlap with the main text. The full theory can be found in ref. [16]. In the moiré pattern, the local bandgap varies in real space and acts as a periodic potential for excitons. Interlayer excitons can be viewed as a wavepacket moving in the potential with a centre-of-mass (COM) motion described by

$$H = \hbar\Omega_0 + \frac{\hbar^2 \boldsymbol{k}^2}{2M} + \Delta(\boldsymbol{r}) \tag{1}$$

$$\Delta(\boldsymbol{r}) = 2V \sum_{j=1,3,5} \cos(\boldsymbol{b}_j \cdot \boldsymbol{r} - \psi) \tag{2}$$

where $\hbar\Omega_0$ is an energy constant, $\hbar^2k^2/(2M)$ is the COM kinetic energy, $\Delta(\boldsymbol{r})$ is the moiré potential energy and M is the exciton mass. For interlayer excitons in a $WSe_2/MoSe_2$ heterobilayer, $M \approx 0.84m_e$, where m_e is the electron bare mass. $\Delta(\boldsymbol{r})$ is a smooth potential and is approximated by the lowest-order harmonic expansion, where $\boldsymbol{b}_j$ are the first-shell moiré reciprocal lattice vectors as shown in Extended Data Fig. 3a. The parameter $V > 0$ is the energy scale of the potential, while Ψ determines where the potential extrema are located. We choose Ψ to be π such that the potential minima are located at R_h^h sites. The reason for this choice is to be consistent with experimental observation, as lowest-energy excitons confined by the potential near the R_h^h site have an s-wave symmetry COM wavefunction and emit σ^+ light at the K valley. Near R_h^h sites, the potential has the form of a harmonic oscillator: $\Delta(\boldsymbol{r}) = -6V + 16\pi^2 V(\frac{r}{a_M})^2/2$, where a_M is the moiré period. An exciton confined in this potential has quantized energy levels: $\sqrt{\frac{16\pi^2 V\hbar^2}{Ma_M^2}}(n_x + n_y + 1)$, where $n_{x,y}$ are non-negative integers. We take the twist angle to be 1°, resulting in a value of a_M of approximately 19 nm. To be consistent with the experimentally observed energy spacing (around 25 meV), we take V to be 18 meV. The overall range of the potential variation is $9V = 162$ meV.

Both +K and −K valley excitons are governed by the Hamiltonian in equation (1), but they have different optical responses due to valley-dependent optical selection rules. Below we focus on +K valley excitons—properties of −K valley excitons can be inferred by using time-reversal symmetry. Following the convention used in ref. [16], the bright interlayer excitons are located at the corners of the moiré Brillouin zone. The optical matrix element for the bright interlayer excitons at the +K valley is:

$$\frac{1}{\sqrt{\mathcal{A}}}\langle G|\hat{\boldsymbol{j}}|\chi_\alpha\rangle = \frac{1}{\mathcal{A}}\int d\boldsymbol{r}\boldsymbol{J}(\boldsymbol{r})u_\alpha(\boldsymbol{r}) \tag{3}$$

$$\boldsymbol{J}(\boldsymbol{r}) = J^+(\boldsymbol{r})\hat{\boldsymbol{e}}^+ + J^-(\boldsymbol{r})\hat{\boldsymbol{e}}^- \tag{4}$$

where $|G\rangle$ is the semiconductor ground state of the heterobilayer, $|\chi_\alpha\rangle$ is the interlayer exciton state, $\hat{\boldsymbol{j}}$ is the in-plane current operator and $\mathcal{A}$ is the system area. In the integral of equation (3), $u_\alpha(\boldsymbol{r})$ is the periodic part of the Bloch wave state $|\chi_\alpha\rangle$, and $\boldsymbol{J}(\boldsymbol{r})$ captures the position dependence of the optical matrix element in the moiré pattern. In equation (4), $\hat{\boldsymbol{e}}^\pm = (1, \pm i)/\sqrt{2}$, and $J^\pm(\boldsymbol{r})$ represent the $\sigma^\pm$ components. The spatial dependence is given by $J^+(\boldsymbol{r}) = \Lambda^+(1 + e^{i\boldsymbol{b}_2\cdot\boldsymbol{r}} + e^{i\boldsymbol{b}_3\cdot\boldsymbol{r}})/3$ and $J^-(\boldsymbol{r}) = \Lambda^-\left[1 + e^{i(\boldsymbol{b}_2\cdot\boldsymbol{r} - \frac{2\pi}{3})} + e^{i(\boldsymbol{b}_3\cdot\boldsymbol{r} + \frac{2\pi}{3})}\right]/3$, where $\Lambda^\pm$ are constants and $|\Lambda^+/\Lambda^-|$ is about 1.33 (ref. [18]). At a generic position, $\boldsymbol{J}(\boldsymbol{r})$ has both σ^+ and σ^- components. There are three notable positions with high symmetry. At the R_h^h site ($\boldsymbol{r} = 0$), J^- vanishes and $\boldsymbol{J}(\boldsymbol{r})$ has a purely σ^+ component. By contrast, at the R_h^X site $\left(\boldsymbol{r} = \frac{a_M}{\sqrt{3}}\hat{\boldsymbol{x}}\right)$, $\boldsymbol{J}(\boldsymbol{r})$ has a purely σ^+ component. Finally, $\boldsymbol{J}(\boldsymbol{r})$ vanishes at the R_h^M site $\left(\boldsymbol{r} = \frac{2a_M}{\sqrt{3}}\hat{\boldsymbol{x}}\right)$. These local optical selection rules are illustrated in Fig. 1b, c. The spatial variation of $J^\pm(\boldsymbol{r})$ is plotted in Extended Data Fig. 3c, d. Around the R_h^h site ($\boldsymbol{r} = 0$), $J^+(\boldsymbol{r})$ is almost constant whereas $J^-(\boldsymbol{r})$ has a vortex structure: $J^-(\boldsymbol{r}) \propto r_x - ir_y$. On the basis of equations (1)–(4), we calculate the theoretical optical conductivity of interlayer excitons at the K valley, as shown in Fig. 4b. We chose $\hbar\Omega_0$ such that the lowest-energy interlayer exciton has the experimental energy 1,310 meV. Four resonances with alternating valley optical selection rules appear in the energy window shown in Fig. 4b. Both the energies and helicities of these resonances agree with the experimental observation. The corresponding exciton centre-of-mass wavefunction can be understood as Bloch wave states composed of Wannier functions confined to the potential minimum position (R_h^h sites). We show $|u_\alpha(\boldsymbol{r})|^2$ for the first three peaks in Fig. 4c–e and for the fourth peak in Extended Data Fig. 3b. For peak 1, $u_1(\boldsymbol{r})$ has s-wave symmetry centred at R_h^h sites, and the integral in

equation (3) acquires only the σ^+ components in $\boldsymbol{J}(\boldsymbol{r})$. In peak 2, the Wannier function associated with $u_2(\boldsymbol{r})$ is still centred at an R_h^h site, but it has a chiral p-waveform with an additional angular momentum compared to $u_1(\boldsymbol{r})$. Owing to this difference, peak 2 has the opposite valley optical selection rule with respect to peak 1. The behaviour of peaks 3 and 4—which have d- and f-waveforms, respectively—can be understood in a similar way.

Thermal behaviour and recombination dynamics. In Extended Data Fig. 4a, we show the steady-state photoluminescence at increased temperatures between 25 K and 70 K. With increasing temperature, the rate at which the intensity of the two highest-energy peaks decreases is considerably faster than that of the lower-energy peaks. Because excitons in the excited states are less confined within the moiré pattern, they are more susceptible to phonon-induced activation out of the potential[41]. Excitons in the excited states can also relax to the lower-energy states, which can enhance the recombination rate from these transitions. Consistent with this we observe a faster decay of the excited states, as shown by the time-resolved photoluminescence dynamics shown in Extended Data Fig. 4b. The dynamics of the highest energy peak is fitted by a single exponential with a time constant of 0.9 ns. As the emission energy decreases, the dynamics become slower and biexponential, approaching decay times of 2 ns and 10 ns for the lowest-energy state. The slight increase in the fast and slow decay times with decreasing energy, shown in the inset to Extended Data Fig. 4b, is often observed in other systems with spatially localized excitons, such as in self-assembled InAs/GaAs quantum dots[42].

Additional heterostructures with interlayer exciton splitting: R-type samples. Here we give additional details about sample 1 (1° twist angle) and sample 2 (2° twist angle) presented in the main text. The Gaussian fit of the photoluminescence spectrum of sample 2 shows the emergence of five interlayer exciton peaks, at 1,306 meV, 1,336 meV, 1,366 meV, 1,386 meV and 1,413 meV. The average energy spacing of sample 2 is 27 ± 3 meV, which is slightly larger than the spacing in sample 1. If we fit this spacing for sample 2 with our model calculation using the same 162-meV moiré potential as for sample 1, we obtain a twist angle of 1.4° from the fit. This value is within our estimated uncertainty in determining the angle via the optical microscopy image of the heterostructure. A larger twist angle causes the lowest-energy transition in a TMD heterobilayer to become more indirect in momentum space[20], leading to a longer recombination lifetime. Indeed, we observe slower time-resolved photoluminescence dynamics for sample 2, shown in Extended Data Fig. 5. Fitting the time-resolved photoluminescence curves with a single exponential function yields time constants of 1.95 ns and 8.96 ns for samples 1 and 2, respectively.

Additional heterostructures with interlayer exciton splitting: H-type samples. We fabricated an H-type heterobilayer (that is, 60° twist angle) that shows two interlayer exciton peaks at 1,356 meV and 1,395 meV (Extended Data Fig. 6). The energy separation between peaks is 40 meV, which is consistent with previous reports of hBN-encapsulated H-type $MoSe_2/WSe_2$ heterobilayers[32]. Our theoretical model predicts that the moiré potential is of the order of 10–20 meV for H-type heterobilayers, which is too small to lead to the observed splitting of 40 meV. In heterobilayers with H-type stacking (twist angle of approximately 60°), the observation of two interlayer exciton resonances separated by 25–50 meV has been attributed to momentum indirect transitions[32] which is consistent with the spectrum of our H-type sample (Extended Data Fig. 6).

Photoluminescence emission from $S_z = 1$ and $S_z = 0$ exciton transitions. A recent theoretical study has also proposed interlayer exciton resonances arising from $S_z = 1$ transitions, which are optically dark in monolayers but become bright in heterobilayers[43]. Although we cannot completely rule out $S_z = 1$ states as a possible explanation for some of the observed resonances, we argue below that such an explanation is less likely for the higher-energy states observed in our study, which are the less-stable states at higher temperature and exhibit a shorter lifetime compared to the lower-energy resonances. In an R-type heterostructure, $S_z = 1$ exciton recombination is predicted to emit left- (right-) circularly polarized light at the R_h^X (R_h^M) atomic configurations. Because the $S_z = 1$ exciton at the K point consists of a spin-down conduction-band electron and spin-up valence-band electron (see Fig. 1b), it emits at an energy higher than that of the $S_z = 0$ states by the conduction-band spin splitting of ~30 meV (see ref. [44]). With increasing temperature, thermalization of excitons might lead to enhanced emission from $S_z = 1$ states, which is inconsistent with the temperature dependence of the excited states shown in Extended Data Fig. 4a. The $S_z = 1$ states are expected to have longer recombination lifetimes than the $S_z = 0$ states owing to a weaker transition dipole moment[43], which is contrary to the trends in the measured lifetimes in Extended Data Fig. 4b. We can also rule out the $S_z = 0$ z-polarized transition because our 50× objective has a small numerical aperture (0.42) compared to the objective with a numerical aperture of 0.82 that was used in a previous study[45] to detect the z-polarized dark exciton in the TMD monolayer. Therefore, we suppress excitation and collection of these states by an additional order of magnitude compared to the in-plane transitions, as shown experimentally in the supplementary material of ref. [45].

Data availability

The data that support the findings of this study are available from the corresponding author upon reasonable request.

34. Kumar, N. et al. Second harmonic microscopy of monolayer MoS_2. *Phys. Rev. B* **87**, 161403 (2013).
35. Malard, L. M., Alencar, T. V., Barboza, A. P. M., Mak, K. F. & de Paula, A. M. Observation of intense second harmonic generation from MoS_2 atomic crystals. *Phys. Rev. B* **87**, 201401 (2013).
36. Wilson, P. T., Jiang, Y., Aktsipetrov, O. A., Mishina, E. D. & Downer, M. C. Frequency-domain interferometric second-harmonic spectroscopy. *Opt. Lett.* **24**, 496–498 (1999).
37. Kresse, G. & Furthmüller, J. Efficient iterative schemes for ab initio total-energy calculations using a plane-wave basis set. *Phys. Rev. B* **54**, 11169–11186 (1996).
38. Kresse, G. & Joubert, D. From ultrasoft pseudopotentials to the projector augmented-wave method. *Phys. Rev. B* **59**, 1758–1775 (1999).
39. Lepetit, L., Chériaux, G. & Joffre, M. Linear techniques of phase measurement by femtosecond spectral interferometry for applications in spectroscopy. *J. Opt. Soc. Am. B* **12**, 2467–2474 (1995).
40. Veenstra, K. J., Petukhov, A. V., de Boer, A. P. & Rasing, T. Phase-sensitive detection technique for surface nonlinear optics. *Phys. Rev. B* **58**, R16020–R16023 (1998).
41. Mouri, S. et al. Thermal dissociation of inter-layer excitons in $MoS_2/MoSe_2$ hetero-bilayers. *Nanoscale* **9**, 6674–6679 (2017).
42. Steinhoff, A. et al. Combined influence of Coulomb interaction and polarons on the carrier dynamics in InGaAs quantum dots. *Phys. Rev. B* **88**, 205309 (2013).
43. Hongyi, Y., Gui-Bin, L. & Wang, Y. Brightened spin-triplet interlayer excitons and optical selection rules in van der Waals heterobilayers. *2D Mater.* **5**, 035021 (2018).
44. Wang, Z., Zhao, L., Mak, K. F. & Shan, J. Probing the spin-polarized electronic band structure in monolayer transition metal dichalcogenides by optical spectroscopy. *Nano Lett.* **17**, 740–746 (2017).
45. Wang, G. et al. In-plane propagation of light in transition metal dichalcogenide monolayers: optical selection rules. *Phys. Rev. Lett.* **119**, 047401 (2017).

a

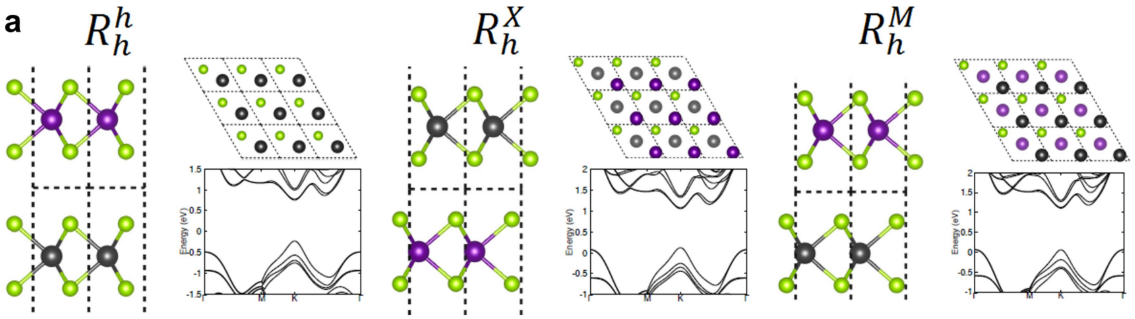

b

	PBE-D2			PBE-D3		
Stacking	R_h^h	R_h^X	R_h^M	R_h^h	R_h^X	R_h^M
W-Mo Interlayer Distance (Å)	7.08	6.44	6.46	7.11	6.52	6.51
Gap at *K* (eV)	1.05	0.93	1.047	1.082	1.032	1.144

c

Stacking	H_h^h	H_h^X	H_h^M	R_h^h	R_h^X	R_h^M
Quasiparticle band gap (eV)	1.58	1.56	1.58	1.58	1.51	1.62
Exciton energy (eV)	1.17	1.17	1.20	1.20	1.12	1.22

Extended Data Fig. 1 | Band structure DFT calculation for different stacking types. a, The three stacking types (R_h^h, R_h^X and R_h^M) of the bilayer $MoSe_2/WSe_2$ heterostructure and corresponding DFT-calculated band structures. **b**, Interlayer distance and bandgap of the three stacking types. **c**, First-principles GW-BSE calculation results for the quasiparticle bandgap and exciton-binding energy of different stacking types.

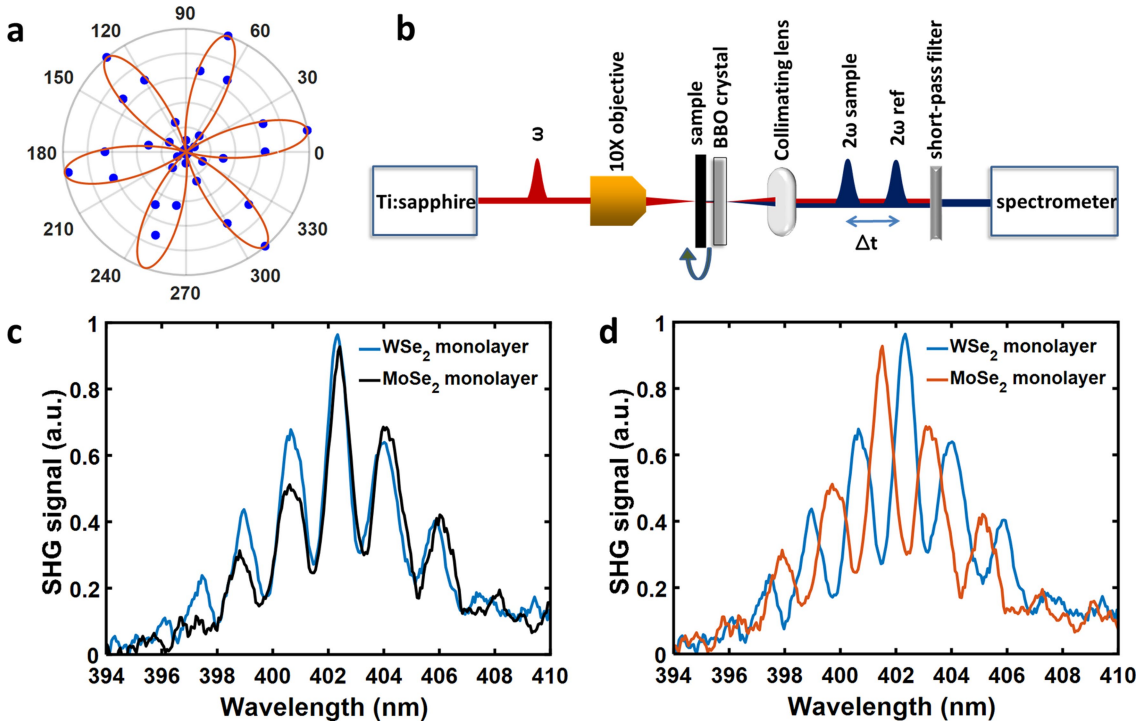

Extended Data Fig. 2 | Second-harmonic generation. a, Polarization-resolved SHG signal as the sample is rotated in a plane normal to the incident laser. The peaks of the SHG signal correspond to the armchair axes of the crystal. **b**, Schematics of the phase-resolved SHG setup. **c**, SHG phase-resolved spectra between the monolayers and the beta barium borate crystal with signals in phase for a twist angle of approximately 0° between the monolayers. **d**, As in **c** but with out-of-phase signals for a twist angle of approximately 60°.

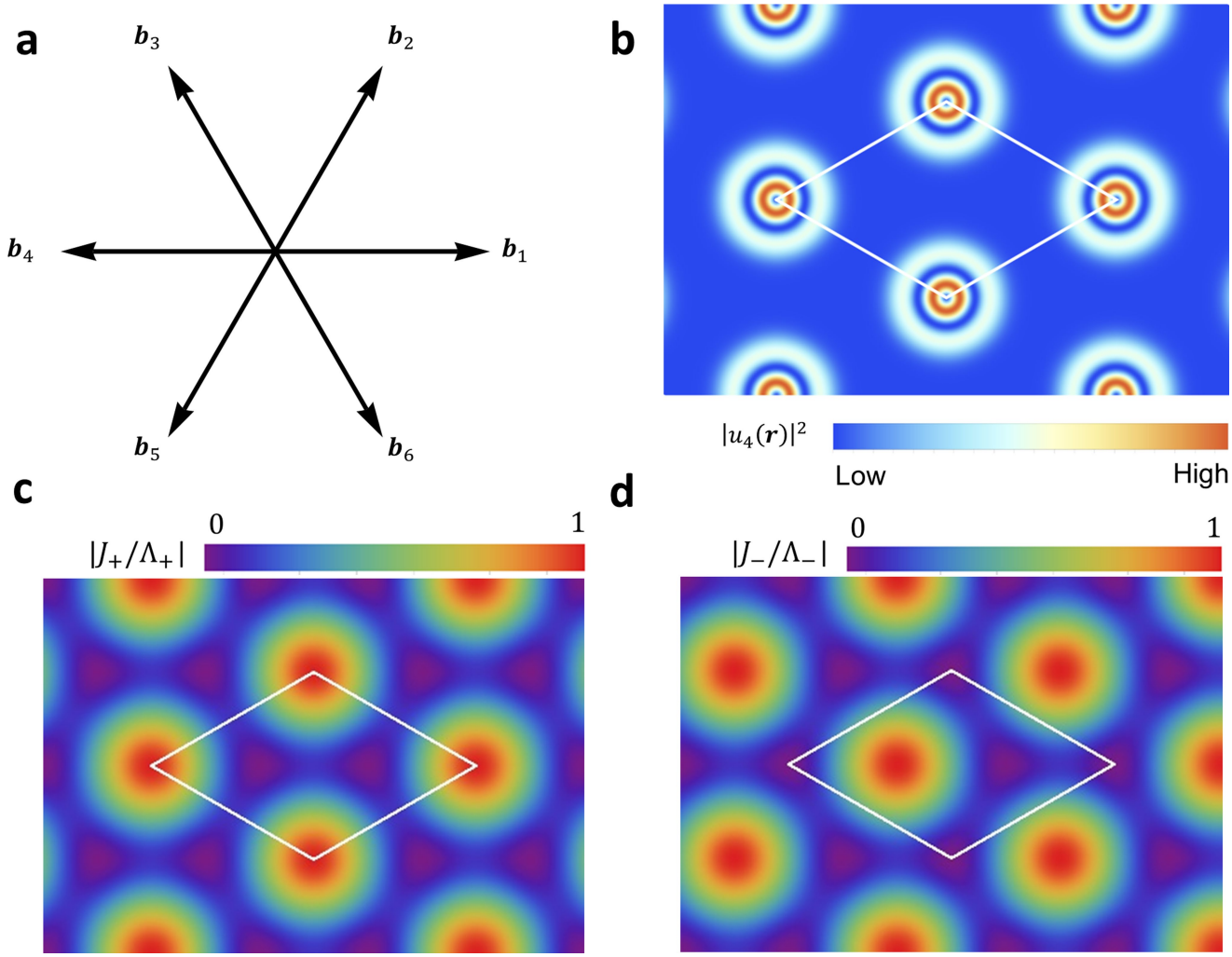

Extended Data Fig. 3 | Moiré exciton theory model. a, Moiré reciprocal lattice vectors in the first shell. **b**, Real-space map of the centre-of-mass wavefunctions for peak 4. **c**, **d**, The spatial variation of the σ^+ (**c**) and σ^- (**d**) components of the optical matrix elements.

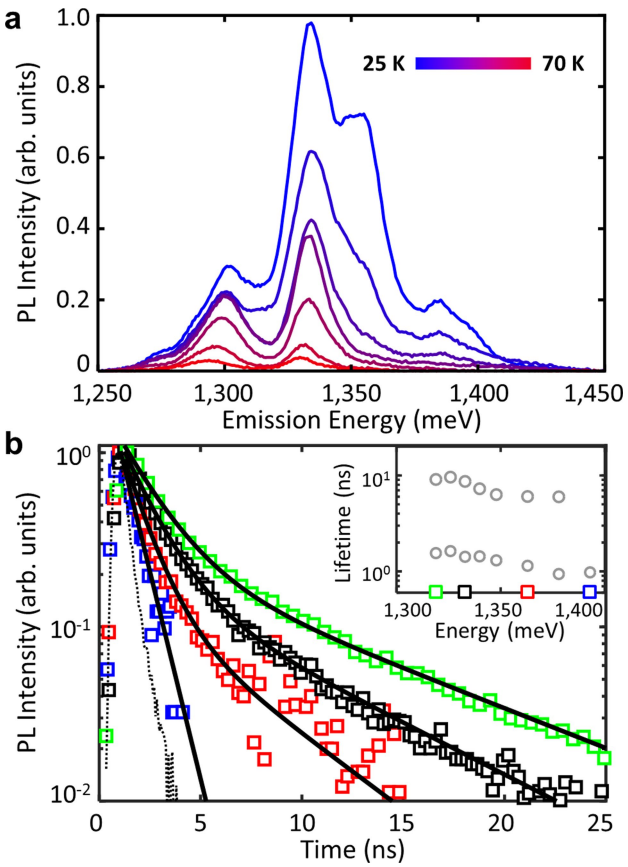

Extended Data Fig. 4 | Thermal decay and recombination dynamics of a heterobilayer with a twist angle of 1°. a, Temperature dependence of the photoluminescence between 25 K and 70 K. **b**, Time-resolved photoluminescence dynamics (points) at energies close to the four interlayer exciton transitions labelled in the inset. The solid lines are biexponential fits to the data. The inset shows the emission energy dependence of the fast and slow decay times.

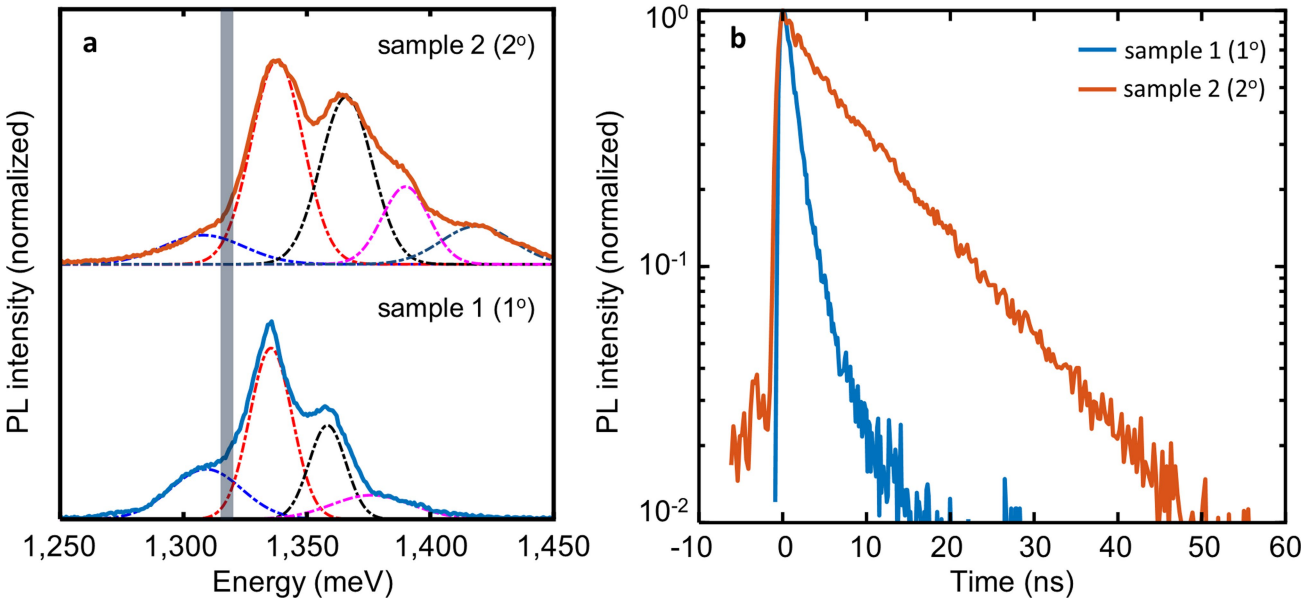

Extended Data Fig. 5 | Comparison of photoluminescence between two heterobilayers with slightly different twist angles. a, Steady-state photoluminescence spectra from the 1° sample (sample 1) and the 2° sample (sample 2). **b**, Time-resolved photoluminescence dynamics for interlayer exciton emission at 1,320 meV, as indicated by the shaded area in **a**.

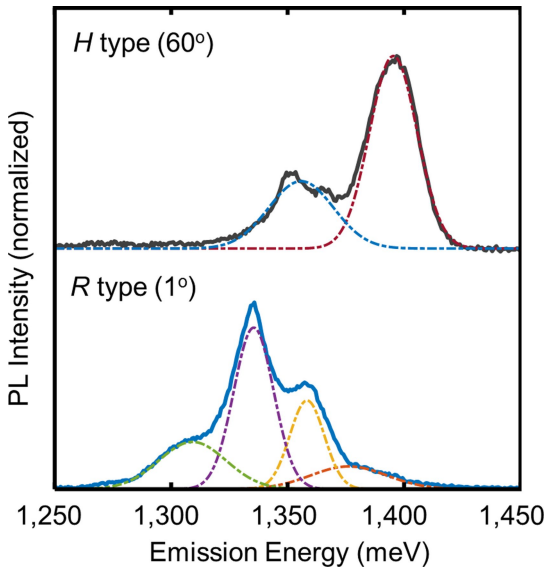

Extended Data Fig. 6 | Spectra from different heterobilayer stacking configurations. Comparison between interlayer exciton resonances from an H-type sample (upper panel) and an R-type sample (lower panel).